Biosensors and Bioelectronics 140 (2019) 111320

Contents lists available at ScienceDirect

Biosensors and Bioelectronics

journal homepage: www.elsevier.com/locate/bios

Self-powered and self-signalled autonomous electrochemical biosensor applied to cancinoembryonic antigen determination

Ana P.M. Tavares[1], Liliana A.A.N.A. Truta[1], Felismina T.C. Moreira, Liliana P.T. Carneiro, M. Goreti F. Sales*

BioMark-CEB/ISEP, School of Engineering, Polytechnic Institute of Porto, Portugal

ARTICLE INFO

Keywords:
Biosensor
Cancer biomarker
Dye-sensitized solar cells
Electrochromic cell
Self-signalled device
Self-powered device

ABSTRACT

This work describes a novel and disruptive electrochemical biosensing device that is self-powered by light and self-signalled by an optical readout. Electrical energy requirements are ensured by a photovoltaic cell that is a dye sensitized solar cell (DSSC), in which one of the electrodes is the biosensing unit. The readout converts electrical energy into colour by an electrochromic cell and signals the concentration dependent event. This device was designed to target a cancer biomarker, cancinoembryonic antigen (CEA).

In brief, the sensing unit was assembled on a conductive glass substrate with a highly conductive poly(3,4-ethylenedioxythiophene) (PEDOT) layer, using a molecularly-imprinted polymer of polypyrrol (PPy) as biorecognition element. This sensing unit acted as the counter electrode (CE) of the DSSC, generating a hybrid device with a maximum power conversion efficiency of 3.45% for a photoanode area of 0.7 cm^2. The hybrid DSSC/biosensor had an electrical output that was CEA concentration dependent from 100 ng/mL to 100 µg/mL, with a limit detection of 0.14 ng/mL in human urine samples. The electrochromic cell consisted of a PEDOT-based material and showed a colour gradient change for CEA concentrations, ranging from 0.1 ng/mL to 100 µg/mL.

Overall, this self-powered and self-signalled set-up is equipment free and particularly suitable for point-of-care analysis (POC), being able to screen CEA in real samples and differentiating critical concentrations for establishing a diagnosis. It holds the potential to provide clinical relevant data anywhere, in a fully independent manner.

1. Introduction

Biosensors based on electrochemical transduction are amongst the most popular devices in biochemical sensing, real-time and *in situ* monitoring(Grieshaber et al., 2008). Typically, electrochemical biosensors signal current and/or potential changes, providing quantitative data about a given target analyte (Arduini et al., 2016; da Silva et al., 2017; Pohanka and Skladai, 2008; Xueji Zhang, 2008). Regardless these attractive features, an electrochemical biosensor needs a power source, normally a battery and an electrical connection between the biosensor and the external reading apparatus. This overall approach may represent a limiting factor for the miniaturization of the complete set-up, due to its dependence in terms of electrical components, such as electrical cables and electronic circuits, thereby increasing the costs and environmental impact of the final product.

Thus, the current technology behind electrochemical biosensors may be improved by generating a self-powered devices (Zhao et al., 2014). To this end, a renewable electrical power source (DSSC) (Oregan and Gratzel, 1991) was merged with a biosensing unit targeting cancer biomarkers (Moreira et al., 2018; Truta et al., 2018). In brief, the CE of the DSSC was modified with a biorecognition element to which a target biomarker would bind, turning the operation of the photovoltaic cell dependent from the concentration of that biomarker. This approach was tested successfully by using both natural (Truta et al., 2018) or plastic (Moreira et al., 2018) antibodies as biorecognition elements. Yet, this self-powered device remained electrically dependent as the electrical output was being measured by a potentiostat.

Aiming to confer full autonomy to the device, a new signalling/transducing element was required. To this end, an electrochromic cell was interfaced in this DSSC/biosensor hybrid set-up. The electrochromic cell generates a colour that is electrically dependent upon application of a given power, typically in a reversible manner In this, an

---

* Corresponding author. BioMark, Sensor Research/ISEP, School of Engineering, Polytechnic Institute of Porto, R. Dr. António Bernardino de Almeida, 431, 4200-072, Porto, Portugal.

E-mail addresses: goreti.sales@gmail.com, mgf@isep.ipp.pt (M.G.F. Sales).

[1] equal first author.

https://doi.org/10.1016/j.bios.2019.111320
Received 15 February 2019; Received in revised form 9 May 2019; Accepted 11 May 2019

electrochromic material changes its colour based on an electrochemically induced redox reaction (Lv et al., 2017; Somani and Radhakrishnan, 2003; Beaujuge and Reynolds, 2010; Fan et al., 2016; Moser et al., 2016). Inorganic materials or organic polymers may be used for this purpose, with organic polymers offering the advantage of a high degree of colour change with easy tuning to new colour requests, and lower potential requirements.

As proof-of-concept, the self-powered and self-signalled device was designed to determine CEA. CEA is an important cancer biomarker and it has been employed in diagnosis of over 90% colorectal cancer (Gao et al., 2018; Hauptman and Glavač, 2017; Zhao et al., 2018). Normally, the detection of CEA is done by serum sample, presenting a normal physiological value between 2.5 ng/mL and 10 ng/mL (Duffy, 2001; Margalit et al., 2018; Nicholson et al., 2016).

Herein, the sensing area of the device consisted in a molecularly-imprinted polymer (MIP) layer to recognize CEA, assembled on a suitable CE support. The MIP layer was formed simply by electropolymerizing pyrrol (Py) monomers in the presence of CEA. In turn, the selection of a suitable CE was critical. Typically, Pt is the preferred material, accounting its great electrocatalyst features, but it is too expensive and prohibits the production of a low cost device (Chen et al., 2017; Hong et al., 2015). In alternative, carbon materials or conductive polymers have been proven successful CEs in DSSCs. Poly(3,4-ethylenedioxythiophene) (PEDOT) in particular shows good conductivity, high transparency, remarkable stability, and low cost, when compared to Pt (Hong et al., 2015; Yoo et al., 2014), and has been selected herein. Thus, the MIP film was assembled on a CE containing a PEDOT layer on Fluorine doped Tin Oxide (FTO) glass.

The hybrid DSSC/Biosensor was set-up with a traditional photoanode of titanium dioxide (TiO_2) with a ruthenium-based dye, an FTO/PEDOT CE containing an imprinted PPy film for CEA on top, and an iodide redox-based electrolyte. The electrochromic cell was interfaced in the external electrical circuit. This cell consisted of a PEDOT-based electrochromic material, a semi-solid electrolyte and an FTO-conductive glass. The overall set-up was optimized with regard to the main critical aspects and tested in the analysis of real samples.

2. Materials and methods

2.1. Equipment and reagents/materials

The list of equipment used in this work is shown in section S1 of the supplementary Material. All chemicals were of analytical grade and water was deionized or ultrapure Milli-Q laboratory grade. The following chemicals were used: Acetic acid glacial (AA, CH_3CO_2H, 100% p.a., Analar Normapur); acetonitrile (ACN, CH_3CN, 99.9%) and sodium dihydrogen phosphate dihidrate (Scharlau); phosphate buffered Saline (PBS) (Amresco); CEA from human fluids, (EastCoast Bio); ethanol absolute (C_2H_6O, $\geq$ 99.9%), (Panreac); hexachloroplatinic (IV) acid hexahydrate ($H_2PtCl_6 \cdot 6H_2O$, ~40% Pt for synthesis) and potassium chloride (Merck); 1-hexyl-3-methylimidazolium iodide (HMII, $C_{10}H_{19}IN_2$, 98%) and 3,4-ethylenedioxythiophene (EDOT, 97%) (Alfa Aesar); iodine (I_2), potassium hexacyanoferrate III ($K_3[Fe(CN)_6]$, potassium hexacyanoferrate II trihydrate ($K_4[Fe(CN)_6]$, sodium phosphate dibasic dihydrate and Sodium acetate (Riedel-de-Häen); lithium iodide (LiI, anhydrous, beads, ~10 mesh, 99.999% trace metals basis), di-tetrabutylammonium cis-bis(isothiocyanato) bis(2,2′-bipyridyl-4,4′-dicarboxylato) ruthenium(II) (N719 dye) and titanium (IV) oxide, anatase nanopowder (TiO_2, 99.7% trace metals basis, < 25 nm), *p*-phenylenediamine and chloroform (Sigma-Aldrich); 4-tert-butylpyridine (TBP, $C_9H_{13}N$, > 96.0%), anhydrous toluene, anhydrous dichloromethane, 1,4-*bis*-2-thienylbutane-1,4-dione and Pyrrole (Py, TCI). The conductive glass substrates used throughout had a conductive film of FTO (sheet resistance 13.0 Ω/sq), and were acquired to Sigma-Aldrich. The electrolyte used in Electrochromic device was a commercial Nafion solution, 20 wt% (contains alcohols) from QUINTECH.

2.2. DSSC assembly and performance

2.2.1. Counter electrode preparation

The DSSC was assembled in a conventional configuration (Fig. S1), for which two different CEs were prepared. These were Pt or PEDOT based, always assembled on FTO/glass as support. First, the FTO area was cleaned by successive ultra-sonication in acetone followed by ethanol and deionized water washing. The active area of the electrode was defined after by applying an insulating film by spin-coating (1700 rpm/20 s) on a circle of 1.0 cm diameter. The subsequent removal of this circle granted an exposed FTO glass area of 1.0 cm diameter. A silver ink was painted in one of the edges of the FTO glass to grant a good electrical contact to this electrode.

The active area of the FTO glass was after covered by Pt or a PEDOT film. For the Pt coverage on top of FTO glass, a platinum salt was dissolved in ethanol and deposited by spin coating at 2000 rpm for 20s. Then, this glass was annealed in the oven at 450 °C for 15 min, resulting in the counter electrode of Pt (Pt CE) (Truta et al., 2019). In the PEDOT CE, this conductive polymer was produced *in-situ* by electropolymerization under a 3-electrode cell (FTO glass acting as working electrode, AgCl/Ag as reference electrode and platinum as counter electrode). The cell was submerged in a solution of 0.01 mol/L of EDOT prepared in aqueous KCl (0.1 mol/L), and was subject to a potential of 1.1 V, for 15 s. It was then washed with ACN to remove exceeding material.

2.2.2. Photoanode preparation

The FTO glass substrate was ultrasonically cleaned in ethanol for 15 min, followed by 15 min in deionized water, and a drying stage in N_2 atmosphere. In parallel, a homogeneous suspension of 6.0 g of TiO_2 anatase nanopowder in 8.0 mL of ethanol absolute, 1.0 mL of acetic acid glacial and in 1.0 mL of ultrapure water, was prepared. This suspension was stirred for 1 h, at room temperature and the resulting paste casted on the clean FTO coated glass, via doctor blade method. Different photoanodes were produced for this purpose, having distinct geometries and areas: rectangular form with an area of 1.40 cm^2, and circular forms with areas of 0.70 and 0.20 cm^2.

The photoanodes were then annealed at 450 °C for 30 min to activate the electronic conduction, cooled down to 80 °C and immersed in a dye solution (5.0×10^{-4} mol/L of N719 in ethanol) for 18 h, at room temperature, in the dark (Chander et al., 2014; Dembele et al., 2013; Hong et al., 2015; Mehmood and Reddy, 2014; Truta et al., 2018). After dye adsorption, the photoanode was removed from the solution, cleaned with ethanol to remove non-adsorbed dye, and dried at room temperature (Hong et al., 2015; Truta et al., 2018).

2.2.3. Assembly and performance

The photoanode and the CE were placed face-to-face, in a sandwich configuration, with a spacer in-between and an iodide-based electrolyte in the middle to close the electrical circuit (Fig. S1). The electrolyte solution contained 0.05 M of I_2, 0.1 M of LiI, 0.6 M of HMII and 0.5 M of TBP, dispersed in ACN. The cell was sealed with a scotch magic tape (double-sided, thickness 19 mm), acting also as a spacer layer between the two electrodes.

The performance of the DSSC was evaluated under a white LED illumination with 100 mW/cm^2 irradiation. The *J–V* features of the cells were recorded in the potentiostat/galvanostat and used to calculate relevant photovoltaic data (overall power efficiency conversion(η); open-circuit potential (V_{OC}); short-circuit voltage(J_{SC}); and fill factor (*FF*)).

2.3. Hybrid DSSC/biosensor

2.3.1. CEA-biosensing film

The biosensing film (Fig. 1A) was obtained by tailoring a MIP layer of Py (MPPy) on the FTO/PEDOT glass electrodes described in section

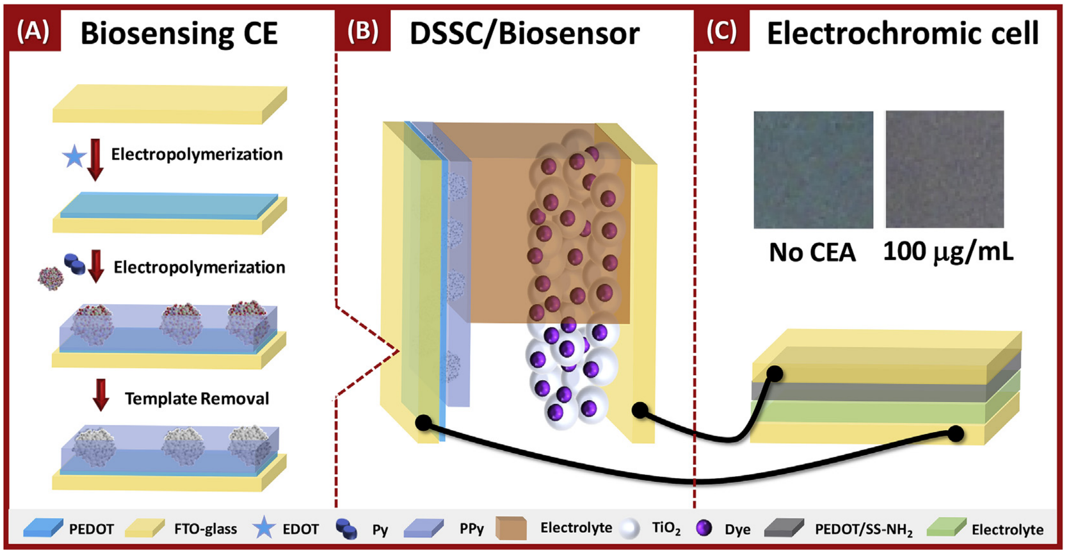

Fig. 1. Schematic representation of the several stages of the biosensing film assembly (A), its integration in the DSSC as the counter electrode to produce the hybrid device (B) and the interface of the external circuit with the electrochromic cell (C).

2.3.1. This was made by electropolymerizing by CV (10 cycles) a Py (5.0×10^{-2} mol/L, in PBS buffer) solution with CEA (0.25 ng/mL), in the 3-electrodes cell. The 3-electrodes cell was the same used to prepare the PEDOT film. CV scans ranged −0.2 to +0.9 V, at a scan-rate of 50 mV/s.

The resulting electrode (FTO/PEDOT/CEA-MPPy) was intensively washed with buffer and incubated for 5 h in proteinase K (500 µg/mL), prepared in PBS buffer, pH 7.4), in the dark, in order to remove the protein template. The final imprinted material (FTO/PEDOT/MPPy) was then rinsed with PBS buffer, to remove peptide fragments and adsorbed proteinase K, and finally rinsed with MQ water. Non-imprinted materials (FTO/PEDOT/NPPy) were produced in parallel using exactly the same procedure, but excluding CEA from it. All these steps were evaluated by electrochemical techniques against an iron redox probe of 0.005 mol/L, prepared in acetate buffer.

2.3.2. *CEA rebinding and electrochemical performance*

The rebinding of CEA was made by incubating buffer, standard solutions or samples in the MPPy area for a given period. Calibrations started by incubating the CEA standard solution of lower concentration in the sensory surface of the electrode, for 15 min (the same time as with the buffer solution), followed by a washing step with buffer. CEA concentrations ranged from 0.1 ng/mL to 100 µg/mL, prepared in acetate buffer, pH 6.0.

After rebinding, the biosensing electrode was combined in a 3-electrodes system to monitor the EIS data changes of a standard iron redox probe. The data reported herein corresponded to a minimum of 3 independent evaluations.

2.3.3. *Assembly of the hybrid system and performance*

The set-up of the hybrid device was similar to the regular DSSC, but the biosensing electrode replaced the normal CE (Fig. 1B). This set-up was made only after incubating the CEA standard solutions or samples in the biosensing film. The performance of the resulting DSSC was evaluated by monitoring EIS and *J-V* data.

2.4. *Electrochromic cell*

2.4.1. *Electrochromic material*

The electrochromic material was generated on the FTO-glass support by electropolymerization of EDOT in the presence of SNS-NH_2, produced as described in section S3 of the Supplementary Material, by following the procedure in Ayranci et al., (2015).

A solution of 2.5×10^{-4} M SNS-NH_2 and 0.1 M EDOT dissolved in 0.1 M $LiClO_4$/0.1 M $NaClO_4$ prepared in ACN was used for this purpose, subject to single CV scanning, between 0.0 V and 1.3 V, at 0.05 V/s. The resulting electrochromic features were evaluated using 0.1 mol/L of KCl as supporting electrolyte, by applying constant external potentials on a 3-electrodes set-up.

2.4.2. *Cell set-up*

The electrochromic cell was set-up by sandwiching face-to-face the FTO-glass with the electrochromic material and another clean FTO-glass, with a polymeric electrolyte (Nafion®) in-between (Fig. 1C).

2.4.3. *Interface in the hybrid DSSC/biosensor*

The electrochromic cell was interfaced in the external circuit linking the photoanode to the CE acting as biosensing film (Fig. 1B and C). It was previously applied to a condition of 0.0 V, forcing the electrochromic material to its neutral state. Under working operation, the white LED of the potentiostat accessory hit the hybrid DSSC/biosensor, thereby generating current that crossed the electrochromic cell and promoted its colour change.

3. Results and discussion

3.1. *Assembly of a suitable DSSC*

A typical DSSC combines CE and photoanode, in electrical contact through a liquid redox iodide-based electrolyte solution, as shown in Fig. S1. The traditional photoanode contains TiO_2 as semiconductor and a suitable dye adsorbed into it; the dye absorbs light and the excited electrons are injected into the conduction band of the semiconductor. The CE is expected to receive the electrons arriving from the photoanode through the external circuit and use these to reduce the redox electrolyte, which in turn would give the electrons back to the dye, regenerating it. As the CE would be the support for the biosensor assembly, it was critical to find-out a compatible structure with both systems (biosensing and DSSC).

3.1.1. *Counter electrode*

Two CEs were prepared and compared herein: the traditional Pt material and a PEDOT layer. The Pt CE was prepared by spin coating deposition, followed by reduction of platinum salt at high temperature.

The PEDOT CE was obtained by chronoamperometry, selecting a potential capable of generating a polymeric structure for a period of 15 s. A potential of +1.1 V was selected, considering that potentials higher than the oxidation peak (Fig. S4) could result in electrochemical degradation, losing properties like conductivity and electroactivity, charge storage ability and poor adhesion to the substrate (Gordon G. Wallace, 2008).

Fig. 2Ashows the photocurrent density-photovoltage (*J-V*) and power conversion efficiency (η) curves obtained for the DSSCs with different CEs (Pt and PEDOT), using the same photoanode and electrolyte. The main photovoltaic parameters were determined from these curves and are summarized in Table S1. Comparing to PEDOT, the Pt CE yielded an increase of 11.1% in η value, and consequently an increment in the overall DSSC parameters: 2.1% V_{OC}, 5.9% in J_{SC}, and 3.4% in *FF*. Yet, a η of DSSC cells with PEDOT CE was also significant, equal to 10.36% due to the good conductivity of this polymer, while reducing significantly the production cost of the final DSSCs (Hong et al., 2015; Yoo et al., 2014). It was also capable of producing a stable response within the purposes of this work, targeting the development of a single use and disposable device. Thus, the PEDOT CE was selected in subsequent studies.

3.1.2. Photoanode

The overall area of the photoanode was considered critical, as studies in the literature linked the efficiency of DSSCs to the photoanode area (Gupta et al., 2008). Moreover, it was of utmost importance to generate enough power to trigger the signalling device, more than to have a highly efficient cell, in which a small area would be efficiently used, but at the expenses of producing low electrical power in absolute terms.

Thus, different areas of photoanodes with a cell containing a PEDOT CE were studied for this purpose: 0.2 cm^2 or 0.70 cm^2. The *J-V* and η curves so obtained are represented in Fig. 2B, and the corresponding photovoltaic parameters (V_{OC}, *FF*, J_{SC} and η) shown in Table S1. Overall, the photoanode area of 0.2 cm^2 yielded the higher η (10.4%) and higher areas of 0.7 cm^2 yielded lower η values (3.5%). Consistently, the J_{SC} densities decreased in 13.3 mA/cm^2 for 0.7 cm^2, when compared to the DSSC-PEDOT cells with 0.2 cm^2 of photoanode area (20.9 mA/cm^2). Likewise, the V_{OC} values decreased with higher photoanodes areas, from 754.1 mV to 752.3 mV (0.7 cm^2). In addition, the *FF* values, representing the photogenerated carriers able to extract out from the photovoltaic device (Qi and Wang, 2013), also decreased with the increasing of area (~7.7%).

Thus, it was clear that the area of the photoanode affected the overall performance of DSSC cell, as it was related to variables affecting the electron transport per unit area and, also, electron recombination (Gupta et al., 2008; Qi and Wang, 2013). Yet, it was also clear that the absolute power generated by the 0.7 cm^2 electrode was significantly higher than that produced by the 0.2 cm^2 photoanode (Fig. 2B). Therefore, it was more likely that the photoanode with larger area would generate enough current to trigger a colour change in the electrochromic cell, thereby allowing a colour change perceptible to naked eye. So, this electrode was selected for further studies.

3.2. Biosensing film production, characterization and rebinding features

3.2.1. Assembly of the film

The assembly of the MIP film was made in several stages, as shown in Fig. 1A, having in mind that it would act as the CE of a DSSC. So, the imprinting was made in the FTO-glass with PEDOT (FTO/PEDOT) by forming a PPy film containing entrapped CEA (FTO/PEDOT/CEA-MPPy), followed by the removal of CEA from this polymeric network (FTO/PEDOT/MPPy) by means of enzymatic action. This was made in parallel with a control non-imprinted film (FTO/PEDOT/NPPy).

3.2.2. Electrochemical follow-up

All stages of the biosensing film assembly were followed by CV in the presence of a standard iron redox probe. The starting material was FTO-glass, which was a conductive support with little ability to catalyse the oxidation or reduction of the redox probe, as reflected in the large potential peak-to-peak separation obtained in the CV assays shown in Figs. S5–A. The subsequent polymerization of the PEDOT on this FTO-glass surface was confirmed by a significant decrease of the observed peak-to-peak separation, as expected for this conductive polymer.

The imprinting stage consisted in the *bulk* electropolymerization of Py in the presence of the target analyte, CEA, made by CV (Fig. S6). The resulting polymeric layer was confirmed by a significant reduction in the net current (Fig. S5-A1), due to the low electron transfer ability of PPy prepared in acetate buffer, pH 6. After the template removal with proteinase K, the oxidation/reduction peaks became more evident, thus supporting the availability of large pores that would enhance the electron transfer and favour the oxidation/reduction of the standard probe and thereby the exit of the protein from the imprinted layer.

In general, the electropolymerization of Py was similar in the presence (MPPy) and in the absence (NPPy) of CEA, considering the CV data (Fig. S6), with the current increasing continuously in subsequent cycles. The non-imprinted film (FTO/PEDOT/NPPy) showed higher peak currents when compared to the MPPy film (FTO/PEDOT/MPPy) after template removal (Fig. S5-A2). This behaviour was linked to the typical capacitive current of PPy. However, the faradaic process

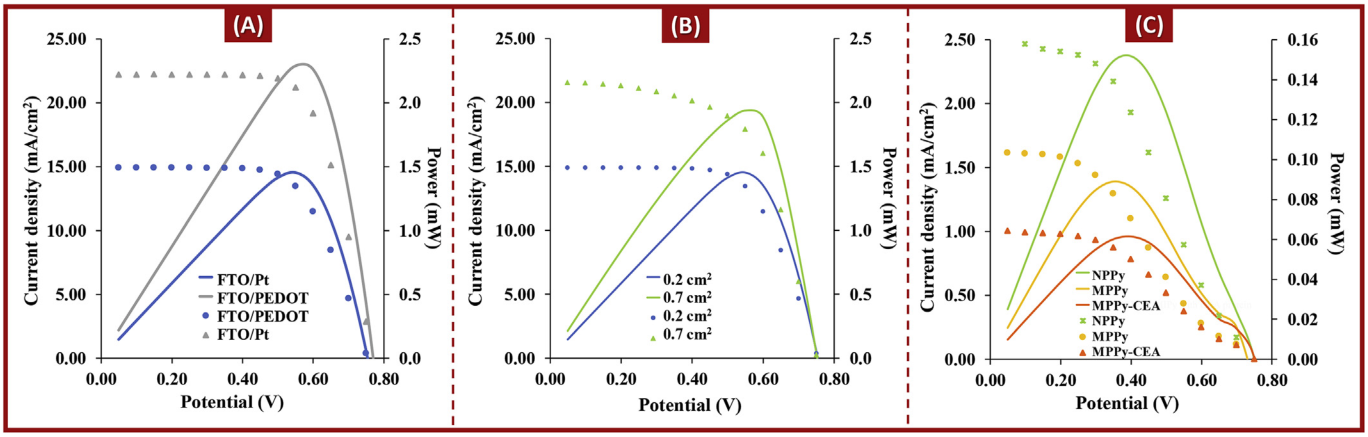

Fig. 2. Photocurrent density-photovoltage (*J-V*) and power conversion efficiency characteristic curves of the DSSCs using different counter electrodes of Pt or PEDOT (A); using photoanodes with different areas (0.2 cm^2 or 0.7 cm^2), for CE of FTO/PDOT (B); and using CEs within the different stages of the production of the sensing film (C).

become slower because the peak separation of the oxidation and reduction peak was higher than in the imprinted sensor. One hypothesis supporting this behaviour was the compactness of the NPPy film, compared to the increased porosity of the MPPy film that accounted the presence of CEA molecules, when the polymeric network was being formed, and their subsequent removal.

EIS assays were also performed along all stages (Figs. S5–B) and were consistent with the CV data. The FTO-glass exhibited an evident resistance to charge transfer (Rct) and, as expected, the presence of PEDOT eliminated this resistance (Xiao-Zi et al., 2010). The formation of a PPy film on the FTO/PEDOT layer recovered some charge transfer resistance, supporting the fact that the MPPy film decreased the electroactive surface area, thereby hindering the electron transfer. After template removal, a more capacitive behaviour was observed, related to the presence of the rebinding cavities. The EIS data also showed higher electron transfer resistance in the NPPy, when compared to the MPPy (Fig. S7), supported by the slower faradaic process observed in this film; the lower porosity of the NPPy would hinder the diffusion of redox active species, thereby increasing R_{ct}.

3.2.3. Raman spectroscopy follow-up

To be sure that the several electrode modifications were effective, the different stages of the film assembly were analysed by Raman spectroscopy (Fig. 3). The presence of PEDOT was clearly evidenced by the strongest intensity peak at 1455.68 cm^{-1}, probably assigned to $C_\alpha = C_\beta$ (-O) symmetric stretching vibration (Chiu et al., 2005; Moraes et al., 2018). Other characteristic peaks of PEDOT were also found. The peak at 988.44 cm^{-1} was assigned to the oxyethylene ring deformation; 1366.44 cm^{-1} to the Cβ-Cβ stretching; 1493.57 cm^{-1} to asymmetric C=C stretching; and 1537.92 cm^{-1} to $C_\alpha = C_\beta$ asymmetric vibration (Garreau et al., 1999). Overall, the Raman spectrum confirmed the presence of PEDOT on top of the FTO-glass electrode.

The addition of a polymeric network of Py to the PEDOT film was recognized by additional Raman peaks. In brief, the NPPy layer yielded typical peaks, at 624.08 cm^{-1} (C–C, ring torsional), 924.37 cm^{-1} (C–C, ring deformation vibration), 1039.63 cm^{-1} and 1073.84 cm^{-1} (C–H in-plane deformation vibration), 1326.17 cm^{-1} (C–C, ring stretching vibration), 1408.09 cm^{-1} (C–N stretching vibration), 1492.09 cm^{-1} (C–C and C=N stretching vibration) and 1599.94 cm^{-1} (C=C in-ring of C–C inter-ring stretching vibrations), thereby confirming the presence of PPy (Gupta, 2008; Lee and Boo, 1996; Stejskal et al., 2016). The structure of the MPPy polymer may be slightly different due to presence of the protein, justifying a wavenumber shift, as confirmed in Table S2 (McStay et al., 2005). Four of these peaks stand out and their intensity ratios were evaluated. Specifically, the ratio of Peaks 1 and 2 confirmed the exit of the protein from the CEA-MPPy film.

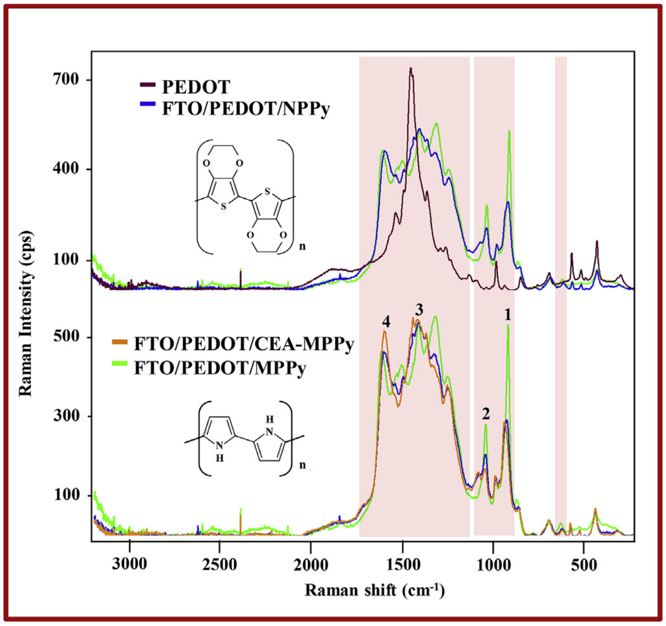

Fig. 3. Raman spectra of the different materials followed along the assembly of the biosensing.

3.2.4. CEA rebinding features

The rebinding features of the biosensor were evaluated by calibration curves with CEA standard solutions. In this, the biosensing film was incubated in each standard solution to evaluate its response in terms of EIS. Calibration curves were recorded for (Glass-FTO/PEDOT/MPPy) and (Glass-FTO/PEDOT/NPPy) (Fig. S8). The calibrations plotted current R_{ct} (in EIS) against CEA concentration, ranging from 0.1 ng/mL to 100 µg/mL.

Overall, the Nyquits plots evidenced linear behaviour for ΔR_{ct} (which $\Delta R_{ct} = R_{ct}(\text{sample})/R_{ct}(\text{blank})$) against log(concentration) from 10 ng/mL to 100 µg/mL of CEA standard solutions prepared in buffer. The linear trend observed among different units was in good agreement when relative data was used (signal ration to the blank value), showing an anionic slope of -0.21 per decade concentration and the squared correlation coefficient > 0.99, presenting an average of relative standard derivation below 6% for all over the concentration range tested ($n = 3$). Interestingly, the NPPy sensor showed a random behaviour with a predominance response for decreasing Rct values. Overall, these results supported that the rebinding mechanism of CEA in the MPPy film was different from that in the NPPy film, being mainly governed by specific interactions at the imprinted sites.

3.3. Self-powered device

The self-powered device consisted in the hybrid DSSC/biosensor set-up (Fig. 1B), using the biosensing film as the CE of the DSSC. In this approach, the biosensing CE was previously incubated in sample for a given time, washed and interfaced in the DSSC to monitor the resulting photovoltaic performance.

3.3.1. Impact of the biosensing film on the DSSC operation

This impact upon the photovoltaic performance of each stage of the sensing film assembly was evaluated first, in order to understand its impact upon the DSSC operation. For this purpose, the *J-V* curves were followed (Fig. 4) and the corresponding photovoltaic parameters (V_{OC}, *FF*, J_{SC} and η) extracted (Table S3).

The use of the FTO/PEDOT as CE yielded a similar behaviour to the control DSSC with the PEDOT-based CE, showing 4.18% η, 791.9 mV V_{OC}, 8.12 mA/cm^2 J_{SC} and 65.0% *FF*. The addition of the CEA-MPPy film (FTO/PEDOT/CEA-MPPy) promoted a significant decrease in η, ~5.3% decrease in V_{OC}, and ~96.4% decrease in J_{SC}, leading to a *FF* value that was 1.6 × lower than the bare DSSC with the FTO/PEDOT CE. This was indeed consistent with the small CV current generated by the MPPy film (Fig. S5). As expected, the removal of CEA from the CE (FTO/PEDOT/MPPy) promoted the opposite effect, increasing the overall η in ~36%. The J_{SC} also increased (0.51 mA/cm^2), but the V_{OC} decreased (22.8 mV), leading to similar *FF* when compared to the previous stage.

The non-imprinted material (FTO/PEDOT/NPPy) was also tested as CE of the DSSC, leading to a higher η value ($\eta = 0.24\%$) when compared to that of the corresponding MPPy ($\eta = 0.15\%$). This was explained by the absence of the protein in the control sensor and was also consistent with the higher currents observed in the CV data (Fig. S5).

3.3.2. CEA rebinding features of the hybrid DSSC/Biosensor

The analytical behaviour of this new set-up was followed by calibrating it with CEA standard solutions of increasing concentrations. Assays were made with standard solutions prepared, first, in acetate buffer (Fig. 4A) and, after, in human urine from healthy individuals,

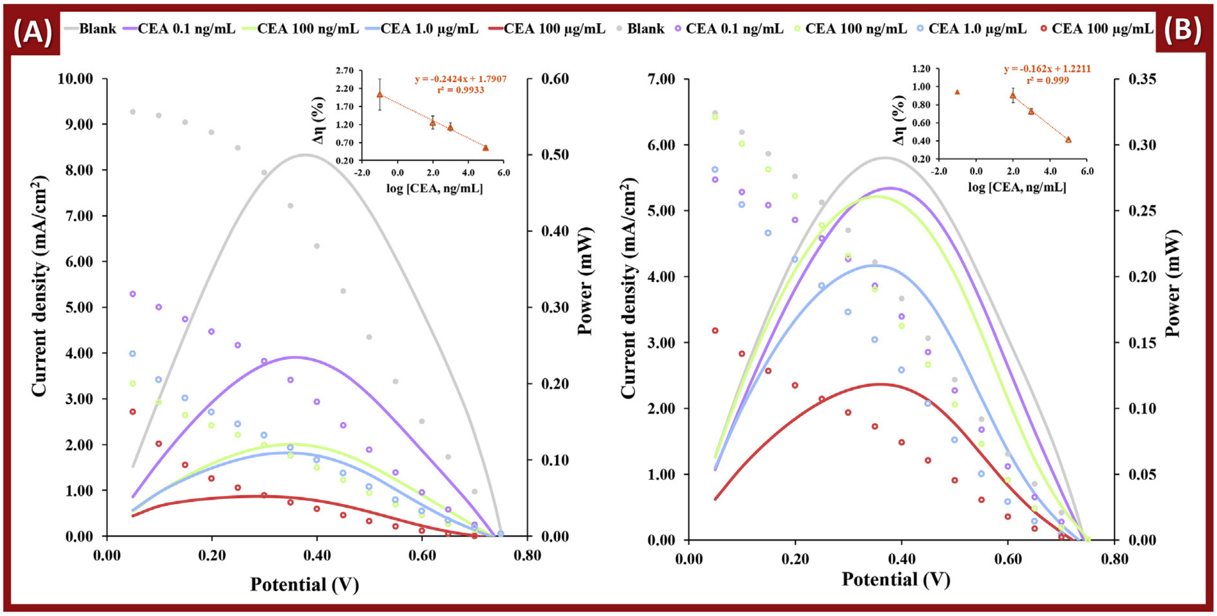

Fig. 4. Typical *J-V* and power conversion efficiency curves of the hybrid DSSC/Biosensing set-up against CEA increasing concentrations in ranging from 0.10 ng/mL to 100.0 µg/mL, prepared in acetate buffer solution (A) or in human urine from healthy individual, diluted 100 × (B), and in the presence of an iodide redox electrolyte. Inset: typical calibration curves plotting the power conversion efficiency against log CEA increasing concentrations.

100 × diluted in buffer (Fig. 4B). The levels of CEA spiked into this blank urine solution ranged from 0.10 ng/mL to 100.0 µg/mL, and the electrochemical behaviour was evaluated by *J-V* measurements, using an iodide redox electrolyte prepared in acetonitrile. In general, the presence of CEA decreased η values (Fig. 4) in a concentration dependent manner. A linear response was observed for $\Delta\eta$ against logarithm CEA concentration, both in acetate buffer conditions and in real urine samples.

After successive incubations (20 min each) with increasing CEA concentrations, the η decreased from 0.31% to 0.09% along the concentration range tested. The typical data so obtained was represented in Fig. 4A, displaying a linear behaviour for Δη against log(CEA concentration), being $\Delta\eta$ equal to $\eta_{(sample)}/\eta_{(blank)}$. The anionic slope obtained was −0.24 per decade CEA concentration and the squared correlation coefficients were > 0.99. The overall change observed for V_{OC} and *FF* values was a decreasing trend with the increasing CEA concentrations, and J_{SC} was the single photovoltaic parameter increasing.

The typical *J-V* and η-based calibration plots obtained in blank human urine samples are shown in Fig. 4B. The higher η value ($\eta = 0.453\%$) was evidenced after stabilizing the hybrid device in blank urine (100 × diluted). Comparing this blank with the blank obtained in acetate buffer, a decrease of η was observed. The $\Delta\eta$ calibration had a linear response from 100 ng/mL until 100 µg/mL, with a slope of −0.16 per decade CEA concentration. The resulting LOD was 0.14 ng/mL, and the squared correlation coefficients were > 0.99. Moreover, repeated calibrations ($n = 3$) indicated that the response was stable and precise, with standard deviations below 9% all over the concentration range tested. Regarding to V_{OC}, J_{SC} and *FF* parameters, an overall tendency to decrease with the increasing of log CEA concentrations was evidenced.

Overall, the response of the hybrid device using the biosensing film as CE of the DSSC was found suitable and its response was CEA concentration dependent. The CEA concentration range to which the hybrid device was providing quantitative information was also of clinical value: < 2.5 ng/mL corresponds to a normal condition and > 10 ng/mL suggests the presence of cancer disease (Duffy, 2001).

3.4. Self-powered and self-signalled device

As the power generated by the hybrid DSSC/biosensor (Fig. 1B) was being concentration dependent and the power reaching a given electrochromic cell is expected to lead to different colour intensities, it was reasonable to infer that different concentrations of CEA would lead to different colour intensities in the electrochromic cell. Thus, a fully autonomous system would be reached, in which the single requirement was light. This possibility was explored first by improving the colours generated by a PEDOT-based electrochromic material and later by interfacing the resulting electrochromic cell in the external electrical circuit of the DSSC/biosensing device (Fig. 1C).

3.4.1. Electrochromic features of the electrochromic material

While the PEDOT holds traditional electrochromic features, it may be modified to improve colour diversity and optical contrast. To this end, SNS-NH_2 was added into it, as suggested in the literature ((Beaujuge and Reynolds, 2010; Lv et al., 2017). The colour changes promoted by this cell were checked under potentiostatic control and in a 3-electrodes cell. As the potential of the a conventional DSSC in blank buffer was never above 0.8 V, the working potential range selected for this test was 0.0–0.8 V.

The pictures obtained after this are shown in Fig. S9 and the resulting colours shown in Fig. 5A, varying from purple to green and blue. In general, these colour reflected the different oxidation states of the materials at each applied potential (Beaujuge and Reynolds, 2010). The contrast observed herein was higher than the one generated by an electrochromic cell having only PEDOT as electrochromic material.

3.4.2. Hybrid DSSC/Biosensor interfaced with the electrochromic cell

This newly developed set-up was tested first in a blank solution and after in increasing CEA concentrations, of 0.1 ng/mL, 100 ng/mL, 1 µg/mL, and 100 µg/mL. This was done by using the same biosensing CE, opening, cleaning and closing it for each subsequent incubation. Time to reach a stable colour in the electrochromic cell was always the same, set to 12 min.

The pictures obtained of the electrochemical cell are shown in Fig. S10 and the colours related to each condition shown in Fig. 5B. In detail, the control signal was generated by the biosensor incubated in

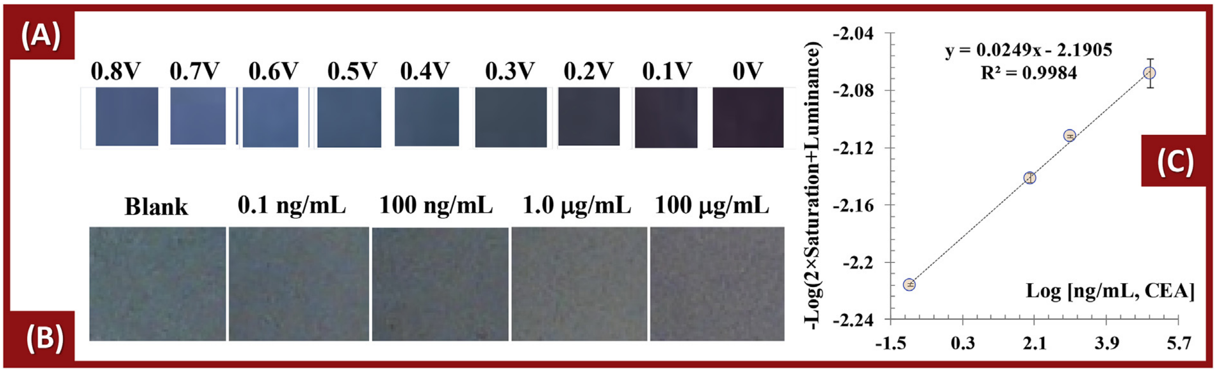

Fig. 5. Coloured behaviour of the electrochromic material when evaluated under a working potential in the 3-electrodes system (A) and when interfaced in the external circuit of the hybrid device DSSC/biosensor (B), with the corresponding calibration (C), generated by plotting the colour coordinates of the HSL coloured space against the logarithm CEA concentration. (For interpretation of the references to colour in this figure legend, the reader is referred to the Web version of this article.)

the blank, corresponding to the highest power produced by the hybrid DSSC/Biosensor device and crossing the electrochromic cell. This blank showed a typical blue colour (Fig. 5B). Increasing CEA concentrations incubated in the CE biosensing film yielded a hybrid device with decreasing currents and, thereby, a purple colour formation of increasing intensity. Overall, it was clear that there was a gradient of colour change that was visually perceptible for increasing CEA concentrations. Moreover, the observed gradient suggested the possibility of obtaining semi-quantitative data by simple visual inspection against a given standard colour palette.

The possibility of extracting quantitative data from the obtained colours was also tested herein, in a similar way to the approach reported by (Gomes and Sales, 2015). To this end, the colour coordinates of the HSL (Hue, Saturation and lightness) colour system were extracted by the Paint program of Windows and mathematically treated. The best mathematical fit found was represented by the y-axis as -Log(2 × Saturation + Luminance) against the log CEA concentration. In this, a linear trend was observed with $y = 0.025$ log [CEA] - 2.19, corresponding to a squared correlation coefficient of 0.99 (Fig. 5C) with RSD less than 1.02% for all over the concentration range tested.

From this study, it was clear that the visual inspection of the colour gradient provided semi-quantitative data and this data could be further refined to generate quantitative information of clinical relevance by handling the colour coordinates.

3.5. Comparison to previously reported CEA sensors

The several MIP materials produced for CEA detection published throughout the years are listed in Table 1. Comparing all transduced signals, the optical detection leads to a linear response within higher concentration ranges, while electrical readings allow a response among lower concentration ranges (sometimes as low as pg/mL in some cases). Overall, the molecular imprinting with optical transducers seems to be unable to achieve concentrations of clinical interest. These reasons may have contributed for a greater number of electrochemical biosensors developed with MIP for CEA sensing, when compared with optical biosensors.

The devices employing electrical detection systems used the electropolymerization technique to obtain the CEA biorecognition element and their results demonstrated a wider linear response and lower limits of detection. However, these methods were based in a conventional electrical dependent biosensing devices and, additionally, different nanomaterials were used to achieve the desired electrochemical features.

Despite the detection limit of this work are not as low as other electrochemical-based works previously reported, the biosensor presented herein showed useful responses for CEA concentration ranges within the values of clinical interest. Moreover, the present work involved an innovative a self-power device that provides semi-quantitative data through visual inspection and quantitative data through a suibtable mathematical handling of the colour coordinated.

4. Conclusions

This work reported a self-powered and self-signalled biosensing device, with sensitivity to very low concentrations, which is a completely novel and disruptive approach. This required merging technology from biosensing, photovoltaic and electrochromic cells. The biosensing device was a low cost MIP material for a cancer biomarker, produced *in situ* and acting as CE of the photovoltaic cell. The photovoltaic cell was a DSSC, inspired in nature and offering advantages in terms of costs. From a practical perspective, DSSC/Biosensor was able to detect to CEA for 0.14 ng/mL, which is an important value for disease screening of colorectal cancer.The electrochromic cell was also a low cost PEDOT-based system produced *in situ*, with significant colour change and low power requirements.

The optimized device yielded a gradient of colour change for increasing CEA concentrations. In general, these varied from blue to purple, with higher concentrations of CEA in the FTO/PEDOT/MPPy CE leading to a more intense purple colour (signalling the lower power

Table 1
Previous works reporting molecularly-imprinted polymers for CEA detection in the literature.

Transduced signal	MIP		LOD	Linear response	Reference
	Material	Technique			
Electrochemical	Pyrrole	Electropolymerization	–	0.05–1.25 pg/mL	Moreira et al. (2016)
Electrochemical	Dopamine	Electropolymerization	<0.26 pg/mL	0.001–1000 ng/mL	Lai et al. (2018)
Electrochemical	Aminophenol	Electropolymerization	3 ng/mL	0.0025–1.5 µg/mL	Truta and Sales (2019)
Optical	Poly(allylamine hydrochloride) and ethylene glycol diglycidyl	Hydrogel-based protein imprinting	–	0.5–125 µg/mL	Casey and Kofinas (2008)

generated by the hybrid DSSC/Biosensor when the CEA concentrations increased). It was clear that the visual inspection of the colour gradient provided semi-quantitative data and this data could be further refined to generate quantitative information of clinical relevance by handling the colour coordinates. The mathematical manipulation of the colour coordinates may be explored in the future, by taking a picture of the observed colour by a smartphone and using a suitable App to generate quantitative data.

Overall, the novel set-up is equipment free and particularly suitable for point-of-care analysis (POC), being able to screen CEA in real samples and differentiating critical concentrations for establishing a diagnosis. It holds the potential to provide clinical relevant data anywhere, in a fully independent manner. Further improvements could be achieved by operating in a DSSC format of higher power, suggesting a wider concentration range of response and a higher sensitivity.

CRediT authorship contribution statement

Ana P.M. Tavares: Investigation, Data curation, Methodology, Validation, Writing - original draft. **Liliana A.A.N.A. Truta:** Investigation, Data curation. **Felismina T.C. Moreira:** Supervision, Investigation, Data curation, Writing - review & editing. **Liliana P.T. Carneiro:** Investigation, Formal analysis. **M. Goreti F. Sales:** Conceptualization, Funding acquisition, Supervision, Project administration, Writing - review & editing.

Acknowledgements

The authors acknowledge the financial support of European Research Council though the Starting Grant, 3P's Starting Grant/ERC (GA 311086).

Appendix A. Supplementary data

Supplementary data to this article can be found online at https://doi.org/10.1016/j.bios.2019.111320.

References

Arduini, F., Micheli, L., Moscone, D., Palleschi, G., Piermarini, S., Ricci, F., Volpe, G., 2016. Trends Anal. Chem. 79, 114–126.

Ayranci, R., Demirkol, D.O., Ak, M., Timur, S., 2015. Sensors 15 (1), 1389–1403.

Beaujuge, P.M., Reynolds, J.R., 2010. Chem. Rev. 110 (1), 268–320.

Casey, B.J., Kofinas, P., 2008. J. Biomed. Mater. Res. A 87A (2), 359–363.

Chander, N., Khan, A.F., Thouti, E., Sardana, S.K., Chandrasekhar, P.S., Dutta, V., Komarala, V.K., 2014. Sol. Energy 109, 11–23.

Chen, R., Yang, C.J., Cai, W.Z., Wang, H.Y., Miao, J.W., Zhang, L.P., Chen, S.L., Liu, B., 2017. ACS Energy Lett. 2 (5), 1070–1075.

Chiu, W.W., Travaš-Sejdić, J., Cooney, R.P., Bowmaker, G.A., 2005. Synth. Met. 155 (1), 80–88.

Dembele, K.T., Nechache, R., Nikolova, L., Vomiero, A., Santato, C., Licoccia, S., Rosei, F., 2013. J. Power Sources 233, 93–97.

Duffy, M.J., 2001. Clin. Chem. 47 (4), 624–630.

Fan, M.S., Kao, S.Y., Chang, T.H., Vittal, R., Ho, K.C., 2016. Sol. Energy Mater. Sol. Cells 145, 35–41.

Gao, Y., Wang, J., Zhou, Y., Sheng, S., Qian, S.Y., Huo, X., 2018. Sci. Rep. 8 (1), 2732.

Garreau, S., Louarn, G., Buisson, J.P., Froyer, G., Lefrant, S., 1999. Macromolecules 32 (20), 6807–6812.

Gomes, H.I.A.S., Sales, M.G.F., 2015. Biosens. Bioelectron. 65, 54–61.

Grieshaber, D., MacKenzie, R., Voros, J., Reimhult, E., 2008. Sensors 8 (3), 1400–1458.

Gupta, S., 2008. J. Raman Spectrosc. 39 (10), 1343–1355.

Gupta, D., Bag, M., Narayan, K.S., 2008. Appl. Phys. Lett. 93 (16).

Hauptman, N., Glavač, D., 2017. Gastroenterol. Res. Pract. 2195361, 11.

Hong, C.K., Ko, H.S., Han, E.M., Park, K.H., 2015. Int. J. Electrochem. Sci. 10 (7), 5521–5529.

Lai, Y., Deng, Y., Yang, G., Li, S., Zhang, C., Liu, X., 2018. J. Biomed. Nanotechnol. 14 (10), 1688–1694.

Lee, S.Y., Boo, B.H., 1996. J. Phys. Chem. 100 (37), 15073–15078.

Lv, X., Li, W., Ouyang, M., Zhang, Y., Wright, D.S., Zhang, C., 2017. J. Mater. Chem. C 5 (1), 12–28.

Margalit, O., Mamtani, R., Yang, Y.-X., Reiss, K.A., Golan, T., Halpern, N., Aderka, D., Giantonio, B., Shacham-Shmueli, E., Boursi, B., 2018. Eur. J. Cancer 94, 1–5.

McStay, D., Al-Obaidi, A.H., Hoskins, R., Quinn, P.J., 2005. J. Opt. A Pure Appl. Opt. 7 (6), S340–S345.

Mehmood, U., Rahman, S., Harrabi, K., Hussein, I., Reddy, B.V., 2014. Adv. Mater.Sci. Eng. (6346), 1–12.

Moraes, B.R., Campos, N.S., Izumi, C.M.S., 2018. Vib. Spectrosc. 96, 137–142.

Moreira, F.T.C., Ferreira, M.J.M.S., Puga, J.R.T., Sales, M.G.F., 2016. Sens. Actuators, B 223, 927–935.

Moreira, F.T.C., Truta, L.A.A.N.A., Sales, M.G.F., 2018. Sci. Rep. 8 (1), 10205.

Moser, M.L., Li, G.H., Chen, M.G., Bekyarova, E., Itkis, M.E., Haddon, R.C., 2016. Nano Lett. 16 (9), 5386–5393.

Nicholson, B.D., Shinkins, B., Mant, D., 2016. J. Am. Med. Assoc. 316 (12), 1310–1311.

Oregan, B., Gratzel, M., 1991. Nature 353 (6346), 737–740.

Pohanka, M., Skladai, P., 2008. J. Appl. Biomed. 6 (2), 57–64.

Qi, B., Wang, J., 2013. Phys. Chem. Chem. Phys. 15 (23), 8972–8982.

Silva, E.T.S.G., Souto, D.E.P., Barragan, J.T.C., de F. Giarola, J., de Moraes, A.C.M., Kubota, L.T., 2017. ChemElectroChem 4 (4), 778–794.

Somani, P.R., Radhakrishnan, S., 2003. Mater. Chem. Phys. 77 (1), 117–133.

Stejskal, J., Trchova, M., Bober, P., Moravkova, Z., Kopecky, D., Vrnata, M., Prokes, J., Varga, M., Watzlova, E., 2016. RSC Adv. 6 (91), 88382–88391.

Truta, L.A.A.N.A., Sales, M.G.F., 2019. Sens. Actuators, B 287, 53–63.

Truta, L.A.A.N.A., Moreira, F.T.C., Sales, M.G.F., 2018. Biosens. Bioelec. 107, 94–102.

Truta, L.A.A.N.A., Pereira, S., Hora, C., Trindade, T., Sales, M.G.F., 2019. Electrochim. Acta 300, 102–112.

Wallace, Gordon G., Geoffrey, P.R.T., Spinks, Leon, M., Kane-Maguire, A.P., 2008. In: Taylor & Francis Group, third ed. CRC Press.

Xiao-Zi, Yuan, Haijiang Wang, C.S., Zhang, Jiujun, 2010. Fundamentals and Applications. Springer-Verlag. London).

Xueji, Zhang, J.W, H.J.a, 2008. Electrochemical Sensors, Biosensors and Their Biomedical Applications. Elsevier.

Yoo, D., Kim, J., Kim, J.H., 2014. Nano Res. 7 (5), 717–730.

Zhao, Y., Deng, P., Nie, Y., Wang, P., Zhang, Y., Xing, L., Xue, X., 2014. Biosens. Bioelectron. 57, 269–275.

Zhao, Q., Zhan, T., Deng, Z., Li, Q., Liu, Y., Yang, S., Ji, D., Li, Y., 2018. Clin. Proteonomics 15, 9,–11.